Revision_1

High-pressure behaviour and atomic-scale deformation mechanisms in inyoite, $CaB_3O_3(OH)_5 \cdot 4H_2O$

Davide Comboni[1], Tommaso Battiston[2], Francesco Pagliaro[2], Paolo Lotti[2], G. Diego Gatta[2], Michael Hanfland[1]

[1] ESRF − European Synchrotron Radiation Facility, 71 Avenue des Martyrs, CS40220, 38043 Grenoble Cedex, France

[2] Dipartimento di Scienze della Terra, Università degli Studi di Milano, Via Botticelli 23, 20133 Milano, Italy

* **Corresponding Author:** Davide Comboni, current email address davide.comboni@esrf.fr

Abstract

The compressional behaviour of inyoite, ideally $CaB_3O_3(OH)_5 \cdot 4H_2O$, has been studied by an *in-situ* high-pressure single crystal X-ray experiment, at the ESRF large scale facility, up to 19.80(5) GPa. Inyoite undergoes a first-order phase transition to inyoite-II, bracketed between 8.25(5) and 8.86(5) GPa, with a large volume discontinuity (ΔV~7.5%). The structure of the high-pressure polymorph has not been solved due to a significant decrease in the number of Bragg reflections. The isothermal bulk modulus ($K_{V0} = \beta^{-1}_{P0,T0}$, where $\beta_{P0,T0}$ is the volume compressibility coefficient) of inyoite was found to be K_{V0} = 26.9(8) GPa, whereas in inyoite-II the K_{V0} value increases to 52(5) GPa. The increase of the bulk modulus is paired with a sharp decrease of the anisotropic compressibility, as shown by the magnitude of the Eulerian finite unit-strain ellipsoid with: ε1:ε2:ε3 = 3.5:2.1:1 in inyoite and ε1:ε2:ε3 =1.5:1.1:1 in inyoite-II. The *P*-induced deformation mechanisms controlling, at the atomic scale, the bulk compression of inyoite are here described on the basis of a series of structure refinements.

1. Introduction

Boron is an important geochemical marker, especially in pegmatitic and granitic systems, for petrogenetic processes despite its low-abundance in the Earth's crust (Barth, 1998; Brenan *et al.*, 1998; Woods, 1994). Highly concentrated, economically sized deposits of boron minerals, always in the form of borates, are relatively uncommon and unevenly distributed in the world, usually in non-marine evaporites associated to hydrothermal activity, in which the most common borates are kernite, borax, colemanite and ulexite (*e.g.*, Turkey; California, USA; Argentina and Bolivia)

(USGS, 2020; Smith & Medrano, 1996; Morgan & Erd, 1969; Helvaci & Alonso, 2000; García-Veigas & Helvaci, 2013). Inyoite is an uncommon borate mineral ($CaB_3O_3(OH)_5 \cdot 4H_2O$, Sp.Gr. $P2_1/n$ with a~10.53 Å, b~12.07 Å, c~8.41 Å, β~112.9° and Z =4, B_2O_3 ~ 37.6 wt%) occurring in prismatic or tabular crystals. Inyoite was initially described by Schaller in the Kramer deposit (Kern County, California, USA) (Schaller, 1916) and its structure was first solved by (Clark, 1959) and later reinvestigated by (Rumanova & Genkina, 1981). In inyoite, the main structural units are isolated $[B_3O_3(OH)_5]^{-2}$ polyions (**Fig. 1**), similarly to those of meyerhofferite ($Ca_2B_6O_6(OH)_{10} \cdot 2H_2O$) and kurnakovite ($MgB_3O_3(OH)_5 \cdot 5H_2O$). Such polyion is formed by two $B\varphi_4$ tetrahedra, which share a corner with a $B\varphi_3$ unit (φ is an anion; O^{2-}or OH^-). These finite clusters of high bond-valence polyedra are usually referred to as "fundamental building blocks" (FBBs) (Hawthorne, 2012). Inyoite structure is formed by finite clusters of polyions connected to Ca-polyhedra and its descriptor, as defined by (Hawthorne, 2012), is $<\Delta 2\square>$, where Δ stands for $B\varphi_3$, $\square$ represents a $B\varphi_4$. The polyions of inyoite are connected to one another through Ca-polyhedra, H_2O molecules and a complex and pervasive hydrogen bond network, which is expected to play a key role in the stability of the crystalline edifice, shown in Fig. 1. Ca is coordinated by eight oxygen atoms to form a distorted polyhedron, which is connected to the two tetrahedra of the polyion through two oxygen hinges (O2 and O7, **Fig. 1**).

Inyoite can be used to synthesize nanomaterials based upon polymerization of borate units, with ferroelectric, pyroelectric or piezoelectric properties (Frost *et al.*, 2015). More in general, borates can act as neutron-shielding materials, due to the isotope ^{10}B (which accounts for about 20% of natural boron) high cross section for thermal neutrons (~3840 barns) leading to the reaction (Carter *et al.*, 1953):

$$^{10}B + n \rightarrow a + {}^{7}Li + \gamma$$

This means that enhanced neutron radiation shielding capacity is achievable by using boron-containing minerals as aggregates in concretes. This could also be the case of inyoite, given its low density (1.87 g/cm^3) and the absence of Na, which is known to induce deleterious processes in Portland concretes, because of the promotion of undesired reactions that undermine the durability of cements (*i.e.*, ''alkali-silica reactions"– ASR) (Thomas, 2011). Furthermore, the use of borates, alongside with other minerals (*e.g.*, magnetite and hematite) as aggregates in concretes, was also reported to attenuate γ-radiations (Glinicki *et al.*, 2018; Amaral *et al.*, 2020; Zayed *et al.*, 2020). Notably, a comprehensive characterization of the crystal-chemistry, elastic parameters, phase-

stability and structural behaviour (at the atomic scale) of inyoite, at different *T* and *P* conditions, is still missing. Recently, the behaviour of a series of natural borates has been studied at non-ambient conditions, with the aim of improving the thermodynamic database of this class of minerals (*e.g*., Lotti et al., 2017, 2018, 2019; Pagliaro *et al.* 2021). High-pressure phase transitions were found in kernite ($Na_2B_4O_6(OH)_2 \cdot 3H_2O$), colemanite ($CaB_3O_4(OH)_3 \cdot H_2O$), kurnakovite ($MgB_3O_3(OH)_5 \cdot 5H_2O$), ulexite ($NaCaB_5O_6(OH)_6 \cdot 5H_2O$) and meyerhofferrite ($CaB_3O_3(OH)_5 \cdot H_2O$), which have structural homologies with inyoite. In particular, meyerhofferite and kurnakovite undergo a phase transition respectively between 3 and 3.5 GPa and 9-11 GPa (Comboni *et al.*, 2020a). Therefore, it is not unreasonable to presume that also inyoite could experience a phase transition at high-pressure, considering that the major difference between meyerhofferite, kurnakovite and inyoite concerns the H_2O content. The thermodynamic/thermoelastic parameters could be useful to model the thermo-mechanical properties of inyoite when used as an aggregate, especially in neutron-shielding concretes as a low-cost alternative of other synthetic B-bearing compounds (*e.g*., B-mullite or B_4C, Gatta et al. 2010, 2013). The characterization at high-pressure of inyoite would allow a comparison with its higher- and lower-H_2O analogues kurnakovite and meyerhofferite, expanding the current knowledge of the deformation mechanisms occurring at high-pressure in hydrated borates.

2. Experimental procedures

The sample of inyoite used in this study was kindly provided by the Museum of Mineralogy- Earth Sciences Dept. University of Milan. A preliminary characterization of the mineral sample was performed by single-crystal X-ray diffraction using a KUMA KM4 four-circle diffractometer (Mo*K*α, point detector), collecting a series of Bragg reflections that were successfully indexed with the unit-cell reported by Clark (1959) and Rumanova & Genkina (1981).

A single crystal of inyoite (~20x15x10μm) was selected for the *in-situ* high-pressure single-crystal synchrotron X-ray diffraction experiment, performed at the ID15b beamline, at the ESRF, Grenoble (France). A convergent monochromatic beam ($E \sim 30$ keV, $\lambda \sim 0.4107$ Å) was used for the diffraction experiment. The diffraction patterns were collected by an *Eiger2 9M CdTe* detector, positioned at about 180 mm from the sample position. Sample-to-detector distance was calibrated using a Si standard and a vanadinite ($Pb_5(VO_4)_3Cl$) crystal. Further details on the beamline setup are reported in (Merlini & Hanfland, 2013). The crystal was loaded in a membrane-driven diamond

anvil cell (DAC), with 600 μm culet Boehler-Almax design anvils, along with a few ruby microspheres as pressure calibrant (pressure uncertainty ± 0.05 GPa (Mao *et al.*, 1986)). A stainless-steel foil (with thickness ~ 250 μm) was pre-indented to 80 μm and then drilled by spark-erosion, leading to a *P*-chamber of ~300 μm in diameter. Helium was used as hydrostatic pressure-transmitting fluid (Klotz *et al.*, 2009). The adopted data collection strategy consisted in a pure ω-scan ($-32<\omega<+32$), with 0.5° step width and 0.25 s exposure time per step. High-pressure data were collected up to about 19 GPa.

3. Data analysis

Indexing of the diffraction peaks and integration of their intensities (corrected for Lorentz-polarization effects) were performed using the *CrysAlisPro* package (Rigaku Oxford Diffraction, 2018). Corrections for X-ray absorption effects (caused by the DAC components) were applied using the semi-empirical *ABSPACK* routine implemented in *CrysAlisPro* (Rigaku Oxford Diffraction, 2018). The structure refinements were performed using the package JANA2006 (Petrícek *et al.*, 2014), in the space group $P2_1/n$, using the atomic coordinates from (Rumanova & Genkina, 1981) as starting model. As common for high-pressure structure refinements, the displacement parameter (D.P.) of all sites was refined as isotropic, in order to decrease the number of variables. No H-sites were located and refined, due to the poor X-ray scattering of H that hinders a reliable evaluation of the positions and displacement parameters of the protons based on high-*P* data. No restraint on bond distances or angles was used.

The unit-cell parameters at high-pressure are listed in Table 1 and their evolution with *P* is shown in Fig. 2, whereas selected diffraction patterns are shown in Fig. 3. The principal statistical parameters of the refinements are listed in Table S1 (deposited as supplementary materials, SM); CIFs (crystallographic information files) have been deposited as Supplementary materials.

Between 8.25(5) and 8.86(5) GPa, inyoite experienced a first-order phase transition to the inyoite-II polymorph, which is metrically monoclinic. As Fig. 3 shows, the Bragg peaks do not violate the reflections conditions dictated by the space group $P2_1/n$, which, therefore, is likely preserved in the inyoite-inyoite-II phase transition. Inyoite-II was found to be stable up to the maximum pressure achieved in this experiment (18.9 GPa). Unfortunately, an abrupt drop in intensity and number of observed reflections (*i.e.*, with $F_o^2 > 3\sigma(F_o^2)$) hindered and ultimately prevented the structure solution of the inyoite-II polymorph: only 110 reflections were detected at 8.86(5) GPa

with respect to the 1658 reflections detected at 8.25(5) GPa. Although enough to obtain, with a reasonable accuracy, the unit cell parameters of inyoite-II, the lack of reflections hindered the solution of the crystal structure of the high-pressure polymorph.

Relevant interatomic distances, average bond lengths, angles, polyhedral volumes, distortion index (defined as $D=\frac{1}{n}\sum_{i=1}^{n}\frac{|l_i-l_{av}|}{l_{av}}$, where l_i is the distance from the central atom to the i^{th} coordinating atom, and $l_{av}$is the average bond length, Baur, 1974) and quadratic elongation (defined as $\langle\lambda\rangle=\frac{1}{n}\sum_{i=1}^{n}\left(\frac{l_i}{l_0}\right)^2$, where l_0 is the center-to-vertex distance of a regular polyhedron of the same volume and l_i is the actual center-to-vertex length, Robinson *et al.*, 1971) have been calculated using the tools implemented in the VESTA software (Momma & Izumi, 2008), and are listed in Table 2 and 3.

The (isothermal) compressional behaviour of the two polymorphs was described using a III- and II- Birch-Murnaghan Equations of State, respectively for inyoite and inyoite-II (BM-EoS; (Birch, 1947)). The BM-EoS allows to refine the bulk modulus (K_{V0} or $K_{P0,T0}$, defined as $-V_0(\partial P/\partial V)_{T0} = \beta^{-1}_{P0,T0}$, where $\beta_{P0,T0}$ is the volume compressibility coefficient at room conditions) and its *P*-derivatives ($K'=\partial K_{P0,T0}/\partial P$ and $K''=\partial^2 K_{P0,T0}/\partial P^2$). Truncated to the second order in energy, *i.e.* with $K'=\partial K_{P0,T0}/\partial P = 4$, the EoS transforms to: $P(fe) = 3K_{P0,T0}\, fe\, (1 + 2fe)^{5/2}$. The BM-EoS parameters (listed in Table 4), were refined minimizing the differences between the EoS curves and the experimental data (weighted by their uncertainties in *P* and *V*), using the *EOS-FIT7-GUI* software (Gonzalez-Platas *et al.*, 2016; Angel *et al.*, 2014). Data were fitted considering an estimated uncertainty of ± 0.05 GPa for pressure (Mao *et al.*, 1986).

4. Results and discussion

The evolution with pressure of the unit-cell parameters of inyoite (shown in Fig. 2 and listed in Table 1) appears to be monotonic up to about 8.25 GPa. At higher pressure, a phase transition (inyoite-to-inyoite-II) occurs. Comparing the unit-cell volume of the low-*P* polymorph at 8.25(5) GPa and that of inyoite-II at 8.86(5) GPa, a difference of about 7.6% is observed (*i.e.*, ΔV~63 Å^3). This is an abrupt decrease of volume, though larger ΔV were detected in other borates (*e.g.*, meyerhofferite, ΔV~10%, Comboni *et al.* 2020a). Inyoite-II is metrically monoclinic and appears to preserve the space group $P2_1/n$ (Fig. 3). In response to the phase transition, the unit-cell edges *a*, *b* and *c* decrease by about 6.2, 1 and 0.7%, respectively. In the low-*P* polymorph, the β

angle decreases from ~112.9° at ambient pressure to ~110° at 8.25(5) GPa. In response to the phase transition, β decreases only slightly to 109.4° (Fig. 2, Tab. 1). In inyoite-II, the behavior of β is not well describable, as the data points suffer of a significant scattering with *P*, though an average horizontal trend can be considered (Fig. 2). The determination of the unit-cell parameters of the high-*P* polymorph is somehow hindered by the low number of observed reflections (110 at 8.86(5) GPa). The elastic parameters, calculated and refined with the *EOS-FIT7-GUI* software revealed that inyoite is a relatively soft mineral, with a bulk modulus of 26.9(8) GPa, whereas inyoite-II is relatively stiffer (K_{V0}~ 52(5) GPa). Similar decrease in the bulk compressibility was observed in other borates *e.g.*, kernite (Comboni *et al.* 2020b) and meyerhofferite (Comboni *et al.* 2020a). From Table 4, it seems that the increase of the bulk modulus is paired with an increase of the anisotropic compressional pattern, being the ratio of the linearized bulk moduli along the principal crystallographic directions K_a:K_b:K_c ~ 1:1:1 in inyoite and 1.5:2.5:1 in inyoite-II. However, since inyoite is a monoclinic mineral, the unit-cell parameter β is not forced to assume any fixed value and it is free to vary with pressure, meaning that the linear bulk moduli along the principal crystallographic directions (listed in Tab. 4) do not allow an exhaustive description of its compressional anisotropy. Thus, the Eulerian finite-strain analysis was performed with the *Win_Strain* software (Angel, 2011), in order to describe magnitude and orientation of the unit-strain ellipsoids for both the polymorphs. The geometrical relationships between the strain ellipsoid and the crystallographic axes of inyoite and inyoite-II can be described by the following matrixes (with ε1>ε2>ε3):

$$\begin{pmatrix}\varepsilon_1\\ \varepsilon_2\\ \varepsilon_3\end{pmatrix} = \begin{pmatrix}161.2(1)^\circ & 90^\circ & 51.1(1)^\circ\\ 90^\circ & 180^\circ & 90^\circ\\ 71.2(1)^\circ & 90^\circ & 38.9(1)^\circ\end{pmatrix} \cdot \begin{pmatrix}a\\ b\\ c\end{pmatrix}$$

for inyoite between 0.0001 and 8.25(5) GPa with ε_1:ε_2:ε_3 = 3.5: 2.1: 1, and

$$\begin{pmatrix}\varepsilon_1\\ \varepsilon_2\\ \varepsilon_3\end{pmatrix} = \begin{pmatrix}75(7)^\circ & 90^\circ & 35(7)^\circ\\ 14.7(1)^\circ & 90^\circ & 124.5(1)^\circ\\ 90(2)^\circ & 0(7)^\circ & 90(5)^\circ\end{pmatrix} \cdot \begin{pmatrix}a\\ b\\ c\end{pmatrix}$$

for inyoite-II between 8.86(5) and 18.91(5) GPa, with ε_1:ε_2:ε_3 =1.5: 1.1: 1. This analysis reverses what otherwise could have been assumed by considering only the linear bulk moduli along the principal crystallographic directions. Overall, the abrupt decrease of the elastic anisotropy is rather impressive. The compressional changes induced by the phase transition resemble the ones

occurring in meyerhofferite (*i.e.*, dramatic decrease of its anisotropic elastic pattern), with which inyoite shares the same framework building units (FBBs) (Comboni *et al.* 2020a).

In order to describe the structure deformation mechanisms occurring in inyoite, an analysis of its hydrogen bond network would be advisable, as it plays a paramount role in the stability of the crystalline edifice. In high-pressure X-ray studies, it is not possible to locate hydrogen atoms, however (Clark, 1959) provides a list of the oxygen-oxygen distances which are entangled *via* hydrogen bonds. On this basis, some conclusions can be drawn by analyzing their evolution with pressure. All the oxygen-oxygen distances decrease steadily with pressure, with only minor differences. The average difference, between the ambient-pressure value and that at 8.25(5) GPa, is ~ 0.18(6) Å (Table 5). Such a decrease is obviously higher, as expected, with respect to the (very minor) shortening of the cation-anion distances (displayed in Table 2). The volumes of the Ca-polyhedra and B-tetrahedra were calculated with the software *VESTA* (Table 2) and their evolution with *P* have been modelled with a second-order Birch-Murnaghan Equation of State (Birch, 1947). Notably, the obtained bulk modulus for the Ca-polyhedra (54(8) GPa, V_0= 25.6(2)) is virtually identical to what calculated in meyerhofferite (55(5) GPa, (Comboni *et al.* 2020a) and double than the bulk modulus of inyoite (Table 4). As the B-tetrahedra are substantially uncompressible (Tab. 2), this leads to the conclusion that the deformation induced by the applied pressure is accommodated, in part by the compression of the Ca-coordination environment and, mainly, through the tilting of the Ca-polyhedra and Bφ_x units around the oxygen hinges and shortening of the H-bonds (Fig. 4). Table 3 reports the most relevant distances and angles of the complex groups formed by Ca polyhedra and the isolated $[B_3O_3(OH)_5]^{-2}$ polyions (Fig.1). Similarly to the oxygen-oxygen distances of the twelve hydrogen bonds, also the selected O-O-O angles display a modest and steady evolution (Table 3, Fig. 4). All the angles reported in Table 3 do not deform dramatically: the difference between the values at ambient pressure and those immediately before the phase transition does not exceed ±2.5°. Also, the length of selected O-O interatomic distances, displayed in Table 3, do not show any major alteration (the maximum Δ is around 0.2 Å). It follows that, as could have been expected, the shortening of the cation-anion distances is only secondary in accommodating the structure deformation, which is mainly governed by deforming the isolated $Ca_2B_6(OH)_{10}(H_2O)_6$ groups (formed by 2 Ca-polyhedra and 2 $[B_3O_3(OH)_5]^{-2}$ polyions) and the hydrogen bond network (Fig. 4). Several attempts were made to collect data at ambient pressure after decompression but, unfortunately, no reflections were found.

5. Concluding remarks and comparison with previous studies

As all the hydrous borates investigated so far at high pressure (Pagliaro et al. 2021, Comboni et al. 2020a, Comboni et al. 2021a, Lotti et al. 2017), even inyoite experiences a *P*-induced phase transition. In inyoite, the transition at high pressure (between 8.3-8.9 GPa) is a first-order and iso-symmetric transformation, which leads to a less compressible high-pressure polymorph (*i.e.*, K_{V0} =26.9(8) GPa for inyoite and 52(5) GPa for inyoite-II). The high-pressure polymorph is less anisotropic if compared to the low-pressure one (*i.e.*, ε1:ε2:ε3 = 3.5: 2.1: 1 for inyoite and $\varepsilon_1:\varepsilon_2:\varepsilon_3$ =1.5: 1.1: 1 for inyoite-II).

From a structural point of view, the $B\varphi_x$ polyhedra in inyoite are organized in finite clusters (Fig. 1 and 4), therefore it is useful to make some comparisons with other borate structures with the same topological features, as *e.g.* kurnakovite, ulexite and meyerhofferite (Fig. 5). In detail, meyerhofferite, inyoite and kurnakovite display the same <Δ2□> finite clusters (Fig. 5), whereas the descriptor of ulexite is <Δ2□> − <Δ2□>. As inyoite shares the same alkali-earth cation of meyerhofferite (*i.e.*, Ca), it is reasonable to assume that the inyoite-to-inyoite-II phase transition is driven by the same high-pressure mechanisms observed in meyerhofferite (Comboni et al. 2021b), *i.e.* the increase in the coordination number of the only boron B site in planar trigonal coordination from III to IV. Such an increase in the B coordination number was observed also in kurnakovite (Pagliaro et al. 2021) and ulexite (Comboni et al. 2021a). Moreover, considering the phase-transition pressure in meyerhofferite (~3.3 GPa), inyoite (~8.6 GPa) and kurnakovite (~10.2 GPa), and their H_2O content (~28, 42 and 49 wt% respectively), it appears that the higher the H_2O content, the higher the pressure at which the phase transition takes place. In fact, it is known that the Lewis acid strength for Ca (0.27 v.u. at ambient conditions) increases with pressure, as it incorporates more electron-donating partners in its first coordination shell. This must be followed by a change of the H_2O and B (0.33 v.u. at ambient conditions) coordination sphere, as differences between Lewis acid and basic strengths are minimized in the most stable structure (Brown 2002, 2009). In this regard, the role of H_2O molecules can be seen as a bond-valence moderator (or bond-strength transformer) (Hawthorne, 2012). Thus, as pressure increases, along with the Lewis acidity of the cation, the number of bonded H_2O has to increase. A good illustration of this phenomenon are the stereochemical differences in H_2O content between inderite $[Mg(H_2O)_4]^{2+}$ (Mg: 0.33 v.u.), inderborite $[CaMg(H_2O)_2]^{4+}$ and meyerhofferite $[Ca(H_2O)]^{2+}$ (Hawthorne, 2012). Furthermore, the

drastic decrease of the observed reflections for the H*P*-polymorph was already observed in meyerhofferite (Comboni et al. 2020b), with which inyoite shares the same FBBs, as a consequence of a first order phase transition, preventing the resolution of the high-pressure polymorph (that was eventually solved by Comboni et al. (2021b) in a further experiment). These considerations lead to the hypothesis that in the inyoite-to-inyoite-II phase transition, the sudden decrease of the unit cell volume is likely ascribable to a change in the coordination environments of the B sites (*i.e.*, CN from 3 to 4).

The *P*-stability of the inyoite, observed in this study, far exceeds the typical working conditions of any concrete. Its bulk modulus (~27 GPa) is lower than what experimentally reported for other hydrated borates used as aggregates (*e.g.*, colemanite ~67 GPa, ulexite ~37 GPa) or of other aggregates usually used in Portland concretes (*e.g.*, calcite ~76 GPa, quartz ~37 GPa). Inyoite is elastically anisotropic, and this is not a positive prerequisite for any potential aggregate. Despite this does imply a preclusion for the utilization of inyoite as a B-bearing aggregate, other more isotropic borates would be preferred.

Acknowledgments

ESRF is thanked for the allocation of the beamtime (10.15151/ESRF-ES-502121336 and 10.15151/ESRF-ES-416429069). GDG, FP, TB and PL acknowledge the support of the Italian Ministry of Education (MIUR) through the projects "PRIN2017 - Mineral reactivity, a key to understand large-scale processes" (2017L83S77) and "Dipartimenti di Eccellenza 2018–2022, Le Geoscienze per la Società: Risorse e loro evoluzione". GDG and PL acknowledge the support of the University of Milano through the project "Piano di Sostegno alla Ricerca 2020". The Editor, C. McCammon, and two anonymous reviewers are thanked for the careful revision of the manuscript. No conflict of interest to declare.

Table 1. Evolution, with pressure, of the unit-cell parameters in inyoite

Table 2: Ca-O and B-O interatomic distances (in Å) and other relevant structural parameters in inyoite.

Table 3: Relevant distances and angles in inyoite (angles in °, distances in Å)

Table 4: Refined elastic parameters pertaining to the different polymorphs of inyoite based on the isothermal III- and II-BM Equation of State fits (*fixed parameter).

Table 5: Oxygen-oxygen distances of the twelve hydrogen bonds as indicated in (Clark, 1959), distances in Å

Table S1 (deposited): Statistical parameters pertaining to the structure refinements of inyoite at different pressures.

Figure 1: The crystal structure of inyoite (Ca-polyhedra in *blue*, B-units in *green*, oxygen atoms in *red* spheres)

Figure 2: Evolution with pressure of the normalized unit-cell parameters and unit-cell volume of inyoite (unit-cell volume in *black* squares, *a* in *blue* circles, *b* in *red* diamonds and *c* in upward *green* triangles). Dashed lines represent the Equation of State (EoS) fits (see text for details). Error bars are smaller than symbols.

Figure 3: Reconstruction, based on the experimental data, of the *0kl*and *hk0* reciprocal lattice planes of inyoite at ambient pressure (*left side*) and in inyoite-II, at 8.86 GPa (*right side*). Although in inyoite-II the number of observed reflections drastically decreases, the systematic extinctions suggest that the space group $P2_1/n$ is preserved.

Figure 4: Evolution, with pressure, of the <Ca-O>, <B-O> and <O···O> distances (Ca-O in *blue* spheres, B1-O in *red* diamonds, B2-O in *black* squares and O···O in *green* triangles)

Figure 5: Comparison between the crystal structure of inyoite $CaB_3O_3(OH)_5{\cdot}4H_2O$, kurnakovite $MgB_3O_3(OH)_5{\cdot}5H_2O$ and meyerhofferite $Ca_2B_6O_6(OH)_{10}{\cdot}2H_2O$ as viewed along *c* (BO_x units in *green*, Ca-polyhedra in *blue*, Mg-polyhedra in *orange*)

References

Amaral LF, Girondi Delaqua GC, Nicolite M, et al (2020) Eco-friendly mortars with addition of ornamental stone waste - A mathematical model approach for granulometric optimization. J Clean Prod 248:119283.

Angel RJ (2011) Win_Strain. A program to calculate strain tensors from unit-cell parameters. http://www.rossangel.com/home.htm. Accessed 01 Sep 2021.

Angel RJ, Gonzalez-Platas J, Alvaro M (2014) EosFit7c and a Fortran module (library) for equation of state calculations. Zeitschrift fur Krist 229:405–419.

Barth S (1998) Application of boron isotopes for tracing sources of anthropogenic contamination in groundwater. Water Res 32:685–690.

Baur WH (1974) The geometry of polyhedral distortions. Predictive relationships for the phosphate group. Acta Crystall B 30:1195-1215.

Birch F (1947) Finite elastic strain of cubic crystals. Phys Rev 71:809–824.

Brenan JM, Ryerson FJ, Shaw HF (1998) The role of aqueous fluids in the slab-to-mantle transfer of boron, beryllium, and lithium during subduction: Experiments and models. Geochim Cosmochim Acta 62:3337–3347.

Brown ID (2009) Recent Developments in the Methods and Applications of the Bond Valence Model. Chem Rev 102: 6858-6919.

Brown ID (2002) The chemical bond in inorganic chemistry. The bond valence model. Oxford University Press, New York

Carter RS, Palevsky H, Myers VW, Hughes DJ (1953) Thermal neutron absorption cross sections of boron and gold. Phys Rev 92:716–721.

Clark JR (1959) Studies of borate minerals. IV. The crystal structure of inyoite, $CaB_3O(OH)_5$ $4H_2O$. Acta Crystallogr 12:162–170.

Comboni D, Pagliaro F, Gatta GD, et al (2020a) High-pressure behavior and phase stability of $Na_2B_4O_6(OH)_2{\cdot}3H_2O$ (kernite). J Am Ceram Soc 103:5291–5301.

Comboni D, Pagliaro F, Gatta GD, et al (2020b) High-pressure behaviour and phase-stability of $Ca_2B_6O_6(OH)_{10}{\cdot}2(H_2O)$ (meyerhofferite). Phys Chem Miner 47, 11.

Comboni D, Pagliaro F, Gatta GD, et al (2021a) Phase transition and high-pressure behavior of ulexite, a potential aggregate in radiation-shielding concretes. Constr Build Mater. 291, 123188

Comboni D, Poreba T, Pagliaro, et al (2021b) Crystal structure of the high-*P* polymorph of $Ca_2B_6O_6(OH)_{10}\cdot 2(H_2O)$ (meyerhofferite). Acta Crystallogr B77, 940-945, doi.org/10.1107/S2052520621009768.

Frost RL, López A, Scholz R, et al (2015) Structural characterization of the borate mineral inyoite - $CaB_3O_3(OH)_5\cdot 4(H_2O)$. J Mol Struct 1080:99–104.

Gatta G.D., Rotiroti N., Fisch M., Armbruster Th. (2010) Stability at high pressure, elastic behavior and pressure-induced structural evolution of ‘‘Al5BO9’’, a mullite-type ceramic material. Phys. Chem. Minerals, 37, 227-236.

Gatta G.D., Lotti P., Merlini M., Liermann H.-P., Fisch M. (2013) High-pressure behavior and phase stability of Al_5BO_9, a mullite-type ceramic material. J. Am. Ceramic Soc., 96, 2583–2592.

García-Veigas J, Helvaci C (2013) Mineralogy and sedimentology of the Miocene Göcenoluk borate deposit, Kirka district, western Anatolia, Turkey. Sediment Geol 290:85–96.

Glinicki MA, Antolik A, Gawlicki M (2018) Evaluation of compatibility of neutron-shielding boron aggregates with Portland cement in mortar. Constr Build Mater 164:731–738.

Gonzalez-Platas J, Alvaro M, Nestola F, Angel R (2016) EosFit7-GUI: A new graphical user interface for equation of state calculations, analyses and teaching. J Appl Crystallogr 49:1377–1382.

Hawthorne FC (2012) A bond-topological approach to theoretical mineralogy: Crystal structure, chemical composition and chemical reactions. Phys Chem Miner 39:841–874.

Helvaci C, Alonso RN (2000) Borate Deposits of Turkey and Argentina; A Summary and Geological Comparison. Turkish J Earth Sci 9:1–27

Klotz S, Chervin JC, Munsch P, Le Marchand G (2009) Hydrostatic limits of 11 pressure transmitting media. J Phys D Appl Phys 42, 7, 075413

Lotti P, Comboni D, Gigli L, et al (2019) Thermal stability and high-temperature behavior of the natural borate colemanite: An aggregate in radiation-shielding concretes. Constr Build Mater 203:679–686.

Lotti P, Gatta GD, Comboni D, et al (2017) High-pressure behavior and P-induced phase transition of $CaB_3O_4(OH)_3\cdot H_2O$ (colemanite). J Am Ceram Soc 100:2209–2220.

Lotti P, Gatta GD, Demitri N, et al (2018) Crystal chemistry and temperature behavior of the natural hydrous borate colemanite, a mineral commodity of boron. Phys Chem Miner 45:405-422

Mao HK, Xu J, Bell PM (1986) Calibration of the ruby pressure gauge to 800 kbar under quasi-hydrostatic conditions. J Geophys Res 91:4673.

Merlni M, Hanfland M (2013) Single-crystal diffraction at megabar conditions by synchrotron radiation. High Press Res 33:511–522

Momma K, Izumi F (2008) VESTA: A three-dimensional visualization system for electronic and structural analysis. J Appl Crystallogr 41:653–658.

Morgan V, Erd R. (1969) Minerals of the Kramer borate district. Calif Calif Div Mines Geol Miner Inf Serv 22:143–153

Pagliaro F, Lotti P, Battiston T, et al (2021) Thermal and compressional behavior of the natural borate kurnakovite, $MgB_3O_3(OH)_5{\cdot}5H_2O$. Constr Build Mater 266, 121094

Petrícek V, Dušek M, Palatinus L (2014) Crystallographic computing system JANA2006: General features. Zeitschrift fur Krist. 229:345–352

Rigaku Oxford Diffraction (2018) CrysAlisPro Software system, version 1.171.38.46.

Robinson K, Gibbs GV, Ribbe PH (1971) Quadratic Elongation: A Quantitative Measure of Distortion in Coordination Polyhedra. Science 172, 567-570

Rumanova IM, Genkina EA (1981) Precise structure of inyoite $CaB_3O_3(OH)_5{\cdot}4H_2O$. Study of hydrogen bonds. Latv Kim Z 643–653

Schaller WT (1916) Inyoite and meyerhofferite, two new calcium borates. US Geol Surv Bull. 610:35–55

Smith G., Medrano M. (1996) Continental borate deposits of Cenozoic age. Rev Mineral. 33:263-298

Thomas M (2011) The effect of supplementary cementing materials on alkali-silica reaction: A review. Cem Concr Res 41:1224–1231.

USGS (2020) Mineral Commodity Summaries 2020. Reston, Virginia (USA)

Woods WG (1994) An introduction to boron: History, sources, uses, and chemistry. Environ Health Perspect 102:5–11.

Zayed AM, Masoud MA, Rashad AM, et al (2020) Influence of heavyweight aggregates on the physico-mechanical and radiation attenuation properties of serpentine-based concrete. Constr Build Mater 260:120473.

Figure 1: The crystal structure of inyoite (Ca-polyhedra in *blue*, B-units in *green*, oxygen atoms in *red* spheres)

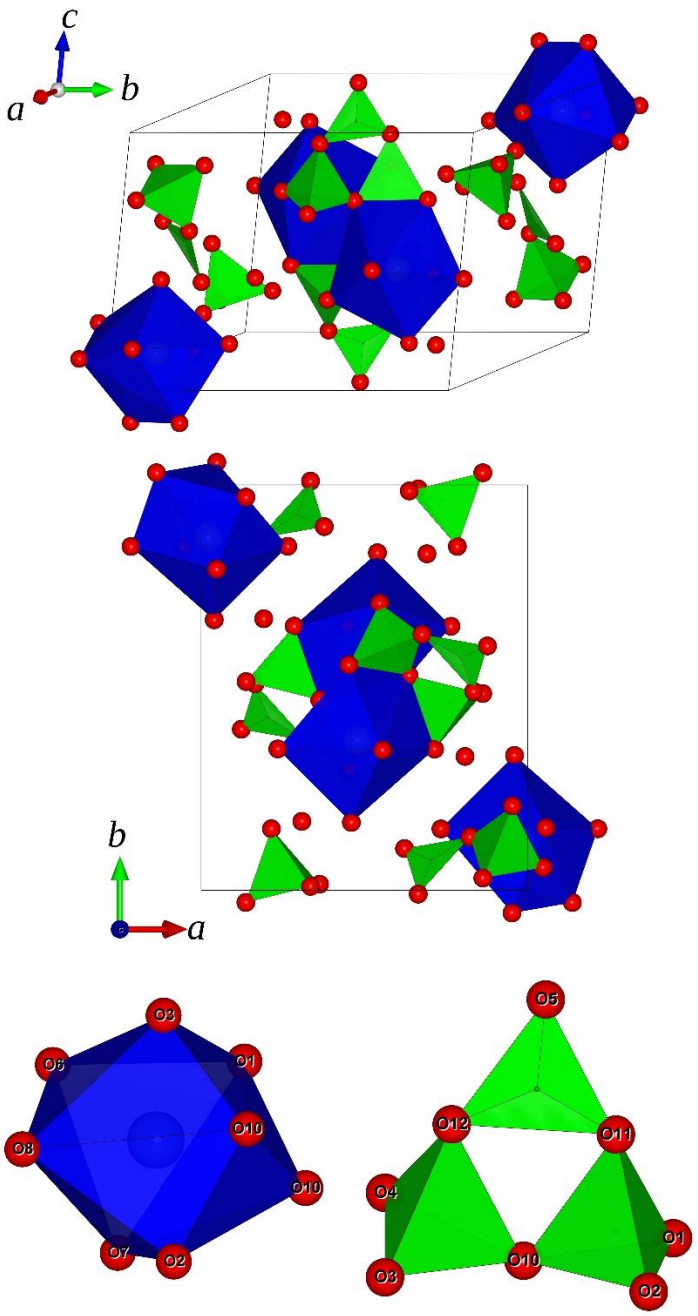

Figure 2: Evolution, with pressure, of the normalized unit-cell parameters and unit-cell volume of inyoite (unit-cell volume in *black* squares, *a* in *blue* circles, *b* in *red* diamonds and *c* in upward *green* triangles). Dashed lines represent the Equation of State (EoS) fits (see text for details). Error bars are smaller than symbols.

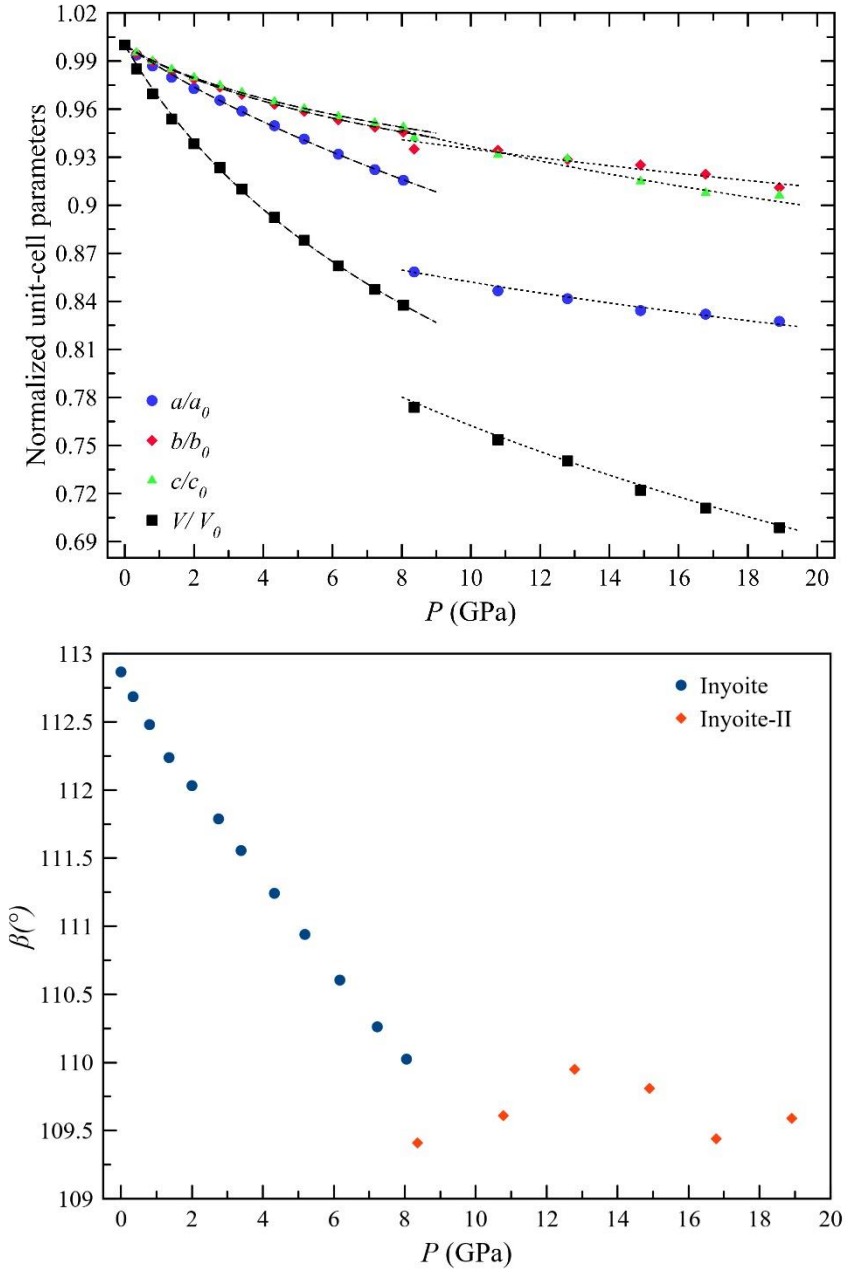

Figure 3: Reconstruction, based on the experimental data, of the *0kl** and *hk0** reciprocal lattice planes of inyoite at ambient pressure (*left side*) and in inyoite-II, at 8.86 GPa (*right side*). Although in inyoite-II the number of observed reflections drastically decreases, the systematic extinctions suggest that the space group $P2_1/n$ is preserved.

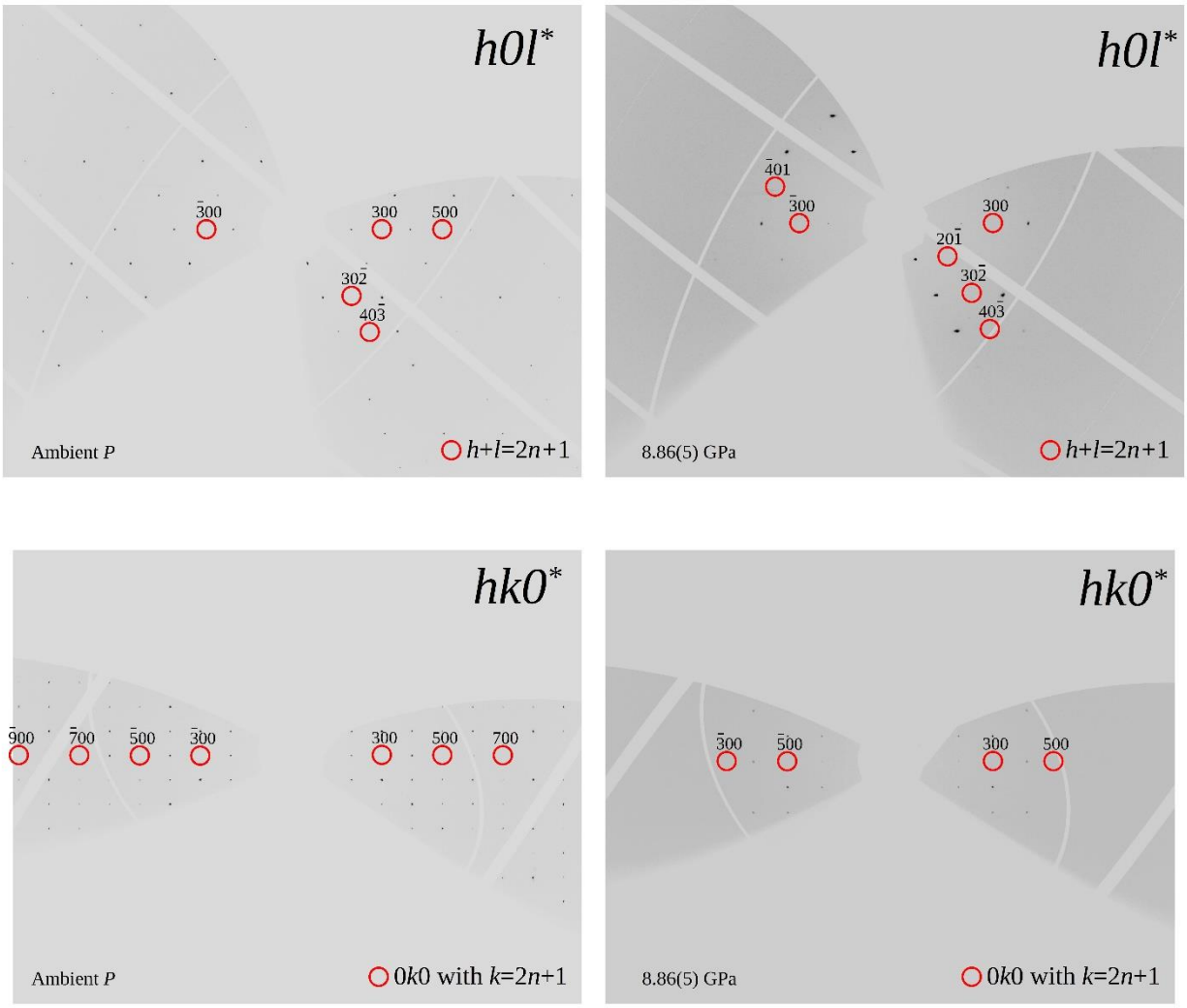

Figure 5: Comparison between the crystal structure of inyoite $CaB_3O_3(OH)_5 \cdot 4H_2O$, kurnakovite $MgB_3O_3(OH)_5 \cdot 5H_2O$ and meyerhofferite $Ca_2B_6O_6(OH)_{10} \cdot 2H_2O$ as viewed along *c* (BO_x units in *green*, Ca-polyhedra in *blue*, Mg-polyhedra in *orange*)

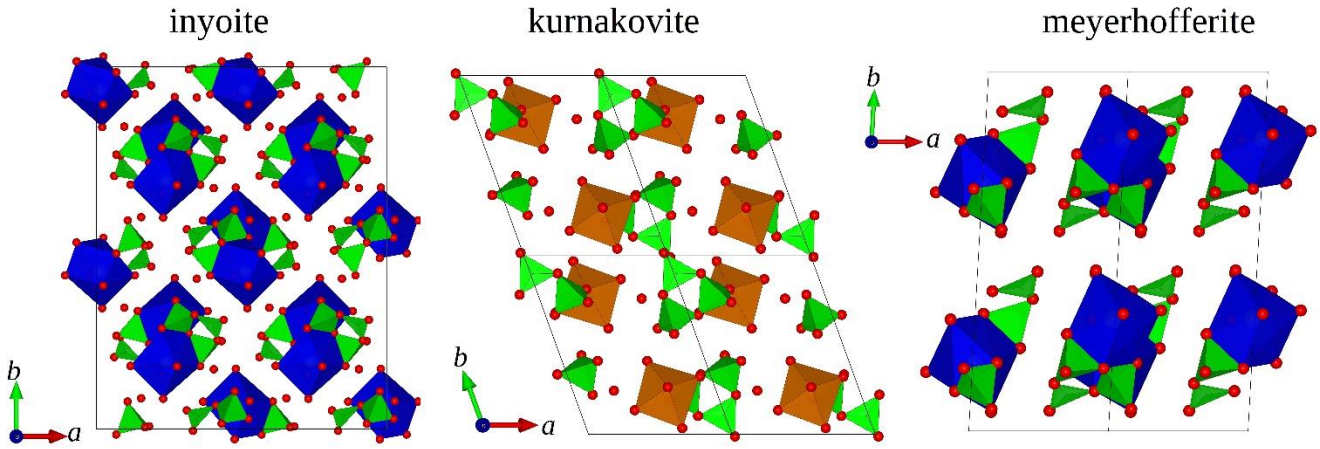

Figure 4: Evolution, with pressure, of the <Ca-O>, <B-O> and <O···O> distances (Ca-O in *blue* spheres, B1-O in *red* diamonds, B2-O in *black* squares and O···O in *green* triangles, σ are smaller than the symbols).

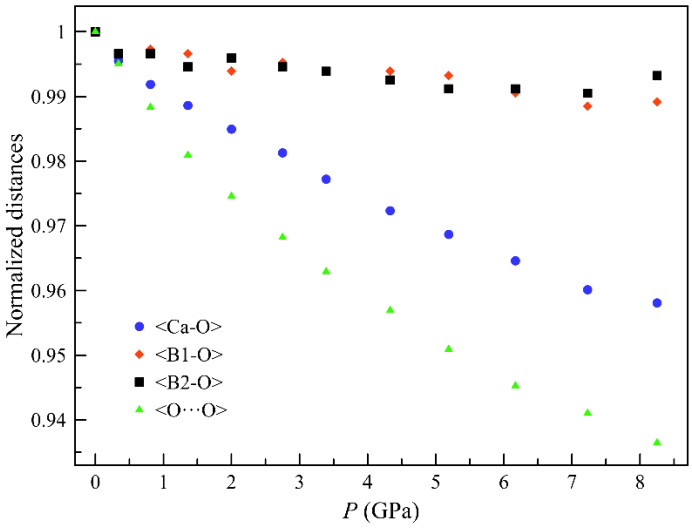

Table 1. Evolution with pressure of the unit-cell parameters in inyoite.

P (GPa)	*a* (Å)	*b* (Å)	*c* (Å)	β (°)	*V* (Å^3)
0.0001	10.5257(4)	12.0742(3)	8.4083(2)	112.867(4)	984.62(6)
0.34(5)	10.4602(5)	12.011(1)	8.3680(3)	112.685(5)	970.0(1)
0.81(5)	10.3878(5)	11.948(1)	8.3236(3)	112.480(5)	954.6(1)
1.36(5)	10.3135(6)	11.879(1)	8.2811(3)	112.238(6)	939.1(1)
2.00(5)	10.2390(5)	11.817(1)	8.2381(3)	112.032(5)	924.0(1)
2.75(5)	10.1622(6)	11.758(1)	8.1958(3)	111.788(6)	909.3(1)
3.39(5)	10.0916(6)	11.702(1)	8.1589(3)	111.556(5)	896.1(1)
4.33(5)	9.9953(5)	11.628(1)	8.1113(3)	111.242(5)	878.7(1)
5.19(5)	9.9077(5)	11.573(1)	8.0737(3)	110.940(5)	864.6(1)
6.17(5)	9.8080(5)	11.511(1)	8.0333(3)	110.605(5)	848.9(1)
7.23(5)	9.7067(5)	11.455(1)	7.9994(3)	110.262(5)	834.4(1)
8.25(5)	9.6368(6)	11.4171(2)	7.9784(2)	110.025(4)	824.75(6)
8.86(5)	9.035(6)	11.29(3)	7.92(1)	109.4(1)	762(2)
10.78(5)	8.911(6)	11.28(5)	7.832(8)	109.5(1)	742(3)
12.79(5)	8.859(4)	11.21(3)	7.81(1)	109.95(9)	729(2)
14.90(5)	8.781(5)	11.17(3)	7.693(6)	109.50(7)	711(2)
16.78(5)	8.757(4)	11.10(2)	7.632(6)	109.44(9)	700(2)
18.91(5)	8.772(9)	11.01(2)	7.64(1)	109.8(1)	694(2)

Table S1 (deposited): Statistical parameters pertaining to the structure refinements of inyoite

P (GPa)	min≤*h*≤max	min≤*k*≤max	min≤*l*≤max	Reflections: total number	Unique reflections	R_1 (obs)	R_1 (all)	wR_1 (obs)	wR_1 (all)	Residuals (e^-/Å^3)
0.0001	-10< *h* <+11	-18< *k* <+17	-11< *l* <+10	2048	1242	0.0643	0.0733	0.0861	0.0881	+0.61;-0.44
0.34(5)	-15< *h* <+14	-11< *k* <+13	-15< *l* <+14	2198	1431	0.0802	0.099	0.1096	0.1158	+0.72;-0.49
0.81(5)	-15< *h* <+14	-11< *k* <+13	-15< *l* <+14	2028	1339	0.0719	0.0903	0.1085	0.1198	+0.88;-0.51
1.36(5)	-14< *h* <+14	-11< *k* <+13	-14< *l* <+14	2128	1390	0.0643	0.0753	0.0929	0.0966	+0.71;-0.50
2.00(5)	-14< *h* <+14	-11< *k* <+13	-14< *l* <+14	2099	1364	0.0674	0.0795	0.0953	0.0986	+0.72;-0.55
2.75(5)	-14< *h* <+14	-11< *k* <+13	-14< *l* <+14	2066	1345	0.0633	0.0777	0.0856	0.0891	+0.78;-0.41
3.39(5)	-14< *h* <+14	-11< *k* <+12	-14< *l* <+14	2134	1356	0.0689	0.0858	0.0965	0.0999	+0.90;-0.43
4.33(5)	-14< *h* <+13	-11< *k* <+12	-14< *l* <+14	1985	1288	0.0629	0.0764	0.0813	0.0843	+0.81;-0.46
5.19(5)	-14< *h* <+13	-11< *k* <+12	-14< *l* <+14	2070	1306	0.0612	0.0769	0.0796	0.0823	+0.68;-0.56
6.17(5)	-14< *h* <+13	-11< *k* <+12	-14< *l* <+13	2053	1294	0.0636	0.0794	0.0824	0.085	+0.80;-0.43
7.23(5)	-14< *h* <+13	-11< *k* <+12	-14< *l* <+13	1998	1269	0.0637	0.0762	0.0831	0.0851	+0.69;-0.52
8.25(5)	-7< *h* <+7	-16< *k* <+17	-10< *l* <+9	1658	1093	0.062	0.067	0.087	0.088	+0.58;-0.53

Table 2: Ca-O and B-O interatomic distances (in Å) and other relevant structural parameters in inyoite.

P(GPa)	0.0001	0.34(5)	0.81(5)	1.36(5)	2.00(5)	2.75(5)	3.39(5)	4.33(5)	5.19(5)	6.17(5)	7.23(5)	8.25(5)
Ca1-O8	2.388(5)	2.377(5)	2.374(4)	2.363(4)	2.357(4)	2.346(4)	2.337(4)	2.333(4)	2.328(4)	2.320(4)	2.314(4)	2.311(4)
Ca1-O3	2.343(5)	2.340(5)	2.331(5)	2.335(4)	2.327(4)	2.329(4)	2.316(5)	2.317(4)	2.311(4)	2.303(4)	2.290(4)	2.285(5)
Ca1-O10	2.516(4)	2.505(5)	2.502(5)	2.490(4)	2.482(4)	2.473(4)	2.466(5)	2.446(4)	2.429(4)	2.436(3)	2.413(4)	2.401(4)
Ca1-O6	2.491(4)	2.464(7)	2.442(7)	2.426(5)	2.415(5)	2.396(5)	2.390(5)	2.366(5)	2.354(5)	2.339(5)	2.328(5)	2.323(3)
Ca1-O1	2.415(4)	2.412(4)	2.414(5)	2.409(4)	2.405(4)	2.404(4)	2.394(4)	2.391(4)	2.393(3)	2.387(4)	2.384(4)	2.383(4)
Ca1-O10	2.557(3)	2.549(4)	2.535(4)	2.529(3)	2.511(3)	2.496(3)	2.481(4)	2.466(3)	2.450(3)	2.420(4)	2.413(3)	2.405(3)
Ca1-O2	2.492(4)	2.480(5)	2.466(5)	2.465(4)	2.457(5)	2.448(5)	2.435(5)	2.421(5)	2.412(4)	2.399(5)	2.382(5)	2.387(4)
Ca1-O7	2.449(5)	2.442(5)	2.434(5)	2.419(4)	2.408(4)	2.394(4)	2.387(4)	2.372(4)	2.360(4)	2.357(4)	2.344(4)	2.335(6)
<Ca-O>	2.457(4)	2.446(5)	2.437(5)	2.429(4)	2.420(4)	2.411(4)	2.401(5)	2.389(4)	2.380(4)	2.370(4)	2.359(4)	2.354(4)
V (Å^3)	25.7(4)	25.4(4)	25.2(4)	25.0(4)	24.7(4)	24.4(4)	24.1(4)	23.8(4)	23.6(4)	23.3(4)	23.0(4)	22.8(4)
D	0.024	0.022	0.020	0.020	0.020	0.019	0.019	0.017	0.017	0.017	0.017	0.017
B2-O10	1.457(7)	1.453(7)	1.446(7)	1.437(6)	1.442(6)	1.452(6)	1.443(7)	1.452(6)	1.452(6)	1.442(6)	1.453(6)	1.448(8)
B2-O3	1.458(7)	1.454(11)	1.465(10)	1.447(8)	1.451(9)	1.438(8)	1.444(9)	1.440(8)	1.434(8)	1.440(8)	1.429(8)	1.449(5)
B2-O4	1.491(9)	1.488(8)	1.480(8)	1.495(6)	1.492(6)	1.486(6)	1.489(7)	1.483(6)	1.484(6)	1.489(6)	1.487(6)	1.478(11)
B2-O12	1.488(6)	1.482(6)	1.486(6)	1.486(4)	1.485(5)	1.486(5)	1.483(5)	1.476(5)	1.474(5)	1.473(5)	1.473(5)	1.481(6)
<B2-O>	1.474(7)	1.469(8)	1.469(8)	1.466(6)	1.468(7)	1.466(6)	1.465(7)	1.463(6)	1.461(6)	1.461(6)	1.460(6)	1.464(7)
V (Å^3)	1.64(2)	1.62(2)	1.62(2)	1.61(2)	1.62(2)	1.61(2)	1.61(2)	1.60(2)	1.60(2)	1.60(2)	1.59(2)	1.61(2)
D	0.011	0.011	0.010	0.017	0.014	0.014	0.015	0.012	0.012	0.014	0.013	0.011
<λ>	1.003	1.003	1.003	1.003	1.003	1.002	1.002	1.002	1.002	1.002	1.002	1.002
B1-O11	1.495(6)	1.479(6)	1.476(6)	1.485(4)	1.479(5)	1.482(5)	1.475(5)	1.486(5)	1.479(5)	1.475(5)	1.468(5)	1.477(6)
B1-O10	1.469(8)	1.472(9)	1.477(9)	1.474(7)	1.465(7)	1.459(7)	1.463(8)	1.467(7)	1.470(7)	1.466(7)	1.460(7)	1.473(8)
B1-O1	1.471(6)	1.464(9)	1.462(10)	1.464(7)	1.462(8)	1.464(8)	1.458(8)	1.456(7)	1.456(7)	1.454(7)	1.456(7)	1.460(5)
B1-O2	1.480(8)	1.482(8)	1.486(8)	1.474(6)	1.476(7)	1.485(7)	1.483(7)	1.472(6)	1.470(7)	1.467(7)	1.462(7)	1.444(10)
<B1-O>	1.479(7)	1.474(8)	1.475(8)	1.474(6)	1.470(7)	1.472(7)	1.470(7)	1.470(6)	1.469(7)	1.465(7)	1.462(7)	1.463(6)
V (Å^3)	1.65(2)	1.64(2)	1.64(2)	1.64(2)	1.63(2)	1.63(2)	1.62(2)	1.63(2)	1.62(2)	1.61(2)	1.60(2)	1.60(2)
D	0.006	0.004	0.004	0.004	0.005	0.007	0.006	0.006	0.004	0.004	0.002	0.008
<λ>	1.002	1.002	1.002	1.002	1.002	1.002	1.002	1.002	1.002	1.001	1.002	1.002

Table 3: Relevant distances and angles in inyoite (angles in °, distances in Å)

P (GPa)	O11-O10-O12	O10-O12-O11	O10-O11-O12	O2-O10-O3	O2-O10-O3
0.0001	58.5(1)	61.1(1)	60.4(1)	81.2(1)	108.9(2)
0.34(5)	58.6(2)	61.3(2)	60.2(2)	81.0(2)	109.2(2)
0.81(5)	58.4(2)	61.0(2)	60.6(2)	81.0(2)	108.7(2)
1.36(5)	58.6(1)	61.2(1)	60.2(1)	80.6(1)	109.4(2)
2.00(5)	58.8(1)	60.9(1)	60.3(1)	80.1(1)	109.4(2)
2.75(5)	58.7(1)	60.9(1)	60.4(1)	80.1(2)	109.4(2)
3.39(5)	58.7(1)	60.8(1)	60.5(1)	79.8(2)	109.2(2)
4.33(5)	58.7(1)	61.0(1)	60.3(1)	79.7(1)	109.5(2)
5.19(5)	58.8(1)	60.9(1)	60.3(1)	79.6(1)	109.8(2)
6.17(5)	59.1(1)	60.7(1)	60.2(1)	79.2(1)	109.7(2)
7.23(5)	59.1(1)	60.5(1)	60.4(1)	79.1(1)	109.2(2)
8.25(5)	59.2(2)	60.5(2)	60.3(2)	78.7(1)	109.5(2)
P (GPa)	O1-O10-O10	O1-O2-O10	O1-O10-O4	O10···O10	O1···O10
0.0001	86.8(1)	80.3(1)	125.5(2)	3.116(4)	3.326(5)
0.34(5)	86.7(2)	80.4(2)	125.6(3)	3.101(4)	3.306(5)
0.81(5)	86.9(2)	80.7(2)	126.0(3)	3.090(4)	3.288(5)
1.36(5)	86.8(1)	80.8(1)	125.7(2)	3.079(3)	3.277(4)
2.00(5)	87.1(1)	81.0(1)	126.0(2)	3.062(3)	3.259(4)
2.75(5)	87.3(1)	81.0(1)	125.9(2)	3.042(3)	3.240(4)
3.39(5)	87.4(1)	81.1(1)	126.2(2)	3.031(3)	3.224(4)
4.33(5)	87.3(1)	81.2(1)	126.2(2)	3.006(3)	3.199(4)
5.19(5)	87.5(1)	81.5(1)	126.1(2)	2.981(3)	3.176(4)
6.17(5)	87.4(1)	81.5(1)	126.5(2)	2.971(3)	3.161(4)
7.23(5)	87.9(1)	81.9(1)	126.8(2)	2.951(3)	3.138(4)
8.25(5)	87.9(2)	81.9(1)	126.5(2)	2.939(5)	3.132(4)

Table 4: Refined elastic parameters of inyoite and inyoite-II, based on the isothermal III- and II-BM Equation of State fits, respectively.

Inyoite	V_0, x_0 (Å^3, Å)	$K_{V0,\,x0}$ (GPa)	K'	$\beta_{V0,\,x0}$ (GPa^{-1})
V	984.6(1)	26.9(8)	6.6(5)	0.037(1)
a	10.5256(9)	22.4(5)	2.7(2)	0.0149(3)
b	12.07313(8)	23.1(9)	9.7(8)	0.0144(7)
c	8.40819(4)	23(1)	12(1)	0.0145(6)

III-BM EoS, P< 8.25 (5) GPa

Inyoite-II	V_0, x_0 (Å^3, Å)	$K_{V0,\,x0}$ (GPa)	K'	$\beta_{V0,\,x0}$ (GPa^{-1})
V	866(11)	52(5)	4*	0.019(2)
a	9.5(1)	43(12)	4*	0.008(2)
b	11.71(8)	73(11)	4*	0.0046(8)
c	8.5(1)	29(8)	4*	0.011(3)

II-BM EoS, P> 8.86(5) GPa

Table 5: Oxygen-oxygen distances of the twelve hydrogen bonds as indicated in (Clark, 1959), distances in Å.

P (GPa)	O4···O6	O6···O12	O2···O8	O4···O7	O5···O7	O9···O11
0.0001	2.891(5)	2.777(4)	2.871(6)	2.753(5)	2.802(6)	2.834(5)
0.34(5)	2.880(7)	2.772(6)	2.868(6)	2.730(6)	2.789(6)	2.805(7)
0.81(5)	2.863(7)	2.766(6)	2.843(6)	2.725(6)	2.758(6)	2.804(7)
1.36(5)	2.835(5)	2.742(5)	2.821(5)	2.700(5)	2.740(5)	2.783(6)
2.00(5)	2.813(5)	2.725(5)	2.804(5)	2.694(5)	2.719(5)	2.771(6)
2.75(5)	2.798(5)	2.707(5)	2.793(5)	2.680(5)	2.693(5)	2.757(6)
3.39(5)	2.774(6)	2.694(5)	2.778(5)	2.667(6)	2.678(5)	2.754(6)
4.33(5)	2.760(5)	2.680(5)	2.766(5)	2.665(5)	2.651(5)	2.729(6)
5.19(5)	2.744(5)	2.668(5)	2.752(4)	2.649(5)	2.635(5)	2.711(6)
6.17(5)	2.729(5)	2.651(5)	2.741(5)	2.641(5)	2.604(5)	2.713(6)
7.23(5)	2.719(5)	2.638(5)	2.737(5)	2.625(5)	2.589(5)	2.694(6)
8.25(5)	2.706(4)	2.618(4)	2.721(5)	2.618(4)	2.600(6)	2.685(4)
P (GPa)	O6···O9	O4···O9	O2···O9	O4···O5	O1···O3	O2···O8
0.0001	2.887(7)	2.761(5)	2.881(6)	2.779(5)	2.880(5)	2.871(6)
0.34(5)	2.879(7)	2.730(7)	2.869(6)	2.759(5)	2.872(6)	2.868(6)
0.81(5)	2.846(7)	2.711(7)	2.839(6)	2.740(5)	2.852(6)	2.843(6)
1.36(5)	2.820(5)	2.704(5)	2.827(5)	2.723(4)	2.821(5)	2.821(5)
2.00(5)	2.795(5)	2.682(5)	2.808(5)	2.699(4)	2.802(5)	2.804(5)
2.75(5)	2.769(5)	2.669(5)	2.789(5)	2.687(4)	2.773(5)	2.793(5)
3.39(5)	2.744(6)	2.654(6)	2.776(5)	2.664(4)	2.768(5)	2.778(5)
4.33(5)	2.717(5)	2.638(5)	2.762(5)	2.644(4)	2.737(5)	2.766(5)
5.19(5)	2.693(5)	2.626(5)	2.746(5)	2.628(4)	2.716(4)	2.752(4)
6.17(5)	2.673(5)	2.601(5)	2.724(5)	2.606(4)	2.701(5)	2.741(5)
7.23(5)	2.654(5)	2.593(5)	2.714(5)	2.591(4)	2.688(5)	2.737(5)
8.25(5)	2.631(7)	2.597(4)	2.691(6)	2.565(6)	2.667(6)	2.721(5)